Chemical Geology 611 (2022) 121124

Contents lists available at ScienceDirect

Chemical Geology

journal homepage: www.elsevier.com/locate/chemgeo

Effects of Mn or Al incorporation on the structure, composition, and As(III) adsorption of oxidized green rust

Xiaoming Wang [a,b,*], Xuewen Li [a], Lanxin Wang [a], Bruno Lanson [c], Mengqiang Zhu [d], Chaoyun Ying [a], Xinran Liang [a], Xionghan Feng [a,b]

[a] Key Laboratory of Arable Land Conservation (Middle and Lower Reaches of Yangtze River), Ministry of Agriculture, College of Resources and Environment, Huazhong Agricultural University, Wuhan 430070, China
[b] State Environmental Protection Key Laboratory of Soil Health and Green Remediation, Wuhan 430070, China
[c] Univ. Grenoble Alpes, Univ. Savoie-Mont Blanc, CNRS, IRD, IFSTTAR, ISTerre, F-38000 Grenoble, France
[d] Department of Ecosystem Science and Management, University of Wyoming, Laramie, WY 82071, United States of America

ARTICLE INFO

Editor: Hailiang Dong

Keywords:
Oxidized green rust
Mn/Al incorporation
Structure
Composition
Elemental distribution
As adsorption

ABSTRACT

The trace cations could incorporate into the structure of oxidized green rust (Ox-GR), a layered reactive Fe(III) oxyhydroxide formed from rapid oxidation of GR, but the effects of cation incorporation on the mineralogical properties and surface reactivity of Ox-GR remain unknown. Here, we synthesized Mn- or Al-incorporated Ox-GR by oxidation of sulfate-bearing GR and determined their structure, elemental composition and distribution, and As(III) adsorption using macroscopic batch experiments and spectroscopic analyses. The presence of Mn or Al favored sulfate accumulation in Ox-GR, with some sulfate being homogeneously distributed in the interlayer, others adsorption on the mineral edge sites. Majority of Mn and Al entered the layer structure of Ox-GR as Mn(III) and Al(III) through isomorphous substitution, leading to the increased d-spacing of (001) plane but slightly decreased d-spacing of a-b planes. The Al incorporation remarkably reduced the structural ordering degree and Fe octahedral layers of Ox-GR through inhibiting the crystal-growth of GR. Compared with the Mn incorporation, the Al incorporation led to a more pronounced structural variation of Ox-GR, ascribed to its higher isomorphic substitution amount. The incorporation of Mn or Al both promoted As(III) adsorption per mineral mass, predominantly due to the increase of sulfate content and/or specific surface area, and the incorporated Mn(III) could oxidize As(III). As(III) adsorption on Ox-GR involved both surface sulfate and > Fe-OH/OH_2 groups exchange, forming a bidentate-binuclear inner-sphere surface complexation. These new insights into the structure and reactivity of Ox-GR are essential to understanding environmental behavior of GR and its derivative Ox-GR in artificial and environmental settings.

1. Introduction

Green Rust (GR) is a layered double hydroxide (LDH) mineral and composed of positively charged Fe(II)-Fe(III)-hydroxide layers with interlayers hosting anions (*e.g.*, SO_4^{2-}) and H_2O molecules (Ruby et al., 2006). The GR has been identified in various environmental settings such as flooded and paddy soils, groundwater, sediments, *etc.*(Trolard and Bourrié, 2006; Trolard et al., 1997), and exerts a strong control on the mobility, toxicity, and redox transformation of organic and inorganic pollutants in those environments (Usman et al., 2018). When exposed to air or contacted with oxidants, GR gradually transforms to goethite, magnetite, and lepidocrocite through dissolution-oxidation-precipitation (DOP) and to oxidized green rust (Ox-GR) through solid-state oxidation (SSO) (Feng et al., 2015; Inoue et al., 2007; Legrand et al., 2004; Refait et al., 2007; Wang et al., 2013).

Ox-GR exhibits a similar layer structure as GR but only contains Fe (III) (Refait et al., 2003). It can form from direct oxidation of GR suspension by strong oxidants such as H_2O_2 (Legrand et al., 2004; Refait et al., 2003) and air oxidation of GR suspension in the presence of oxyanions (*e.g.*, phosphate, silicate, or arsenate) (Feng et al., 2015; Refait et al., 2007; Wang et al., 2017). The key process of the formation of Ox-GR through GR oxidation is the stabilization of the layer structure

* Corresponding author at: Key Laboratory of Arable Land Conservation (Middle and Lower Reaches of Yangtze River), Ministry of Agriculture, College of Resources and Environment, Huazhong Agricultural University, Wuhan 430070, China.
E-mail address: wangxm338@mail.hzau.edu.cn (X. Wang).

https://doi.org/10.1016/j.chemgeo.2022.121124
Received 12 July 2022; Received in revised form 15 September 2022; Accepted 15 September 2022
Available online 21 September 2022

by oxyanion adsorption on the edge sites (Feng et al., 2015; Legrand et al., 2004; Wang et al., 2017). The reactive oxygen species (ROS) with strong oxidation ability and oxyanion inhibitors (*e.g.*, phosphate and silicate) are ubiquitous in natural environments (Cruz et al., 2013; Tong et al., 2016), which provides suitable conditions for the formation of Ox-GR through GR oxidation. Previous studies relevant to Ox-GR mainly focused on the synthesis of single-sheet Ox-GR with dodecanoate stabilizing the structure of GR (Ayala-Luis et al., 2010; Huang et al., 2013; Yin et al., 2019a) and its use as adsorbent to efficiently remove arsenate and phosphate from wastewater (Barthelemy et al., 2012; Yin et al., 2019b). In addition, Ox-GR could serve as an electron accepter for Fe reducing bacteria and directly transform to GR (Jorand et al., 2007). However, the structure, composition, and surface reactivity of Ox-GR are still poorly understood.

The cations of Al and Mn are abundant in natural environments and can enter the structure of Fe (oxyhydr)oxides through isomorphous substitution, changing their structure and surface activity (Cornell and Schwertmann, 2003). Naturally occurring GR usually contains trace cations through adsorption and/or co-precipitation (Genin and Ruby, 2004; Johnson et al., 2014; Johnson et al., 2015). A lot of studies have indicated that the Al(III) ions can replace Fe(III) in the layer of GR during its formation, thereby remarkably decreasing the crystallinity and coherent scattering domain size, varying the cell parameters, and favoring its transformation to goethite (Dideriksen et al., 2022; Genin and Ruby, 2004; Refait et al., 2017; Ruby et al., 2008; Trolard and Bourrié, 2006). In contrast, the effect of Mn on the crystallization of GR depends on its concentration, *i.e.*, low Mn concentration slightly favors its crystallization but high Mn concentration slightly inhibits (Wang et al., 2019); the presence of Mn promotes the formation of lepidocrocite and magnetite during GR transformation (Inoue et al., 2007; Wang et al., 2019). Therefore, when the Al- or Mn-bearing GR was rapidly oxidized to Ox-GR, the incorporation of Al or Mn in Ox-GR will undoubtfully change the structure and composition of Ox-GR, which needs to be clarified.

Additionally, GR is one of the most effective Fe (oxyhydr)oxides for arsenic (As) sequestration in the anoxic subsurface environments (Perez et al., 2020; Perez et al., 2019; Perez et al., 2021; Su and Wilkin, 2005), and the As(III) and As(V) uptake by GR are substantially affected by the pH and coexisting ions (Perez et al., 2019). The transformation of GR in the presence of As(V) can greatly accumulate As(V), leading to the formation of Ox-GR at high As(V) loadings (Wang et al., 2017). Adsorption of As(V) onto single-sheet Ox-GR is very fast, with 80% of total As(V) adsorbed within 10 min, and involves protonated and deprotonated bidentate inner-sphere complexes (Yin et al., 2019b), but the As(III) adsorption behavior on Ox-GR and what are the effects of Mn or Al incorporation remain unknown.

The objectives of this study are, therefore, to determine the effects of Mn or Al incorporation on the structure, elemental composition and distribution, and As(III) adsorption behaviors of the Ox-GR. To reach these aims, we firstly synthesized the Mn- and Al-incorporated Ox-GR samples by rapid oxidation of sulfate-bearing GR with the presence of Mn or Al. The structure, composition, elemental speciation and distribution of these Ox-GR samples were then characterized by X-ray diffraction (XRD), Fourier transform infrared (FTIR) spectroscopy, high-resolution transmission electron microscopy (HRTEM) combined with selected area electron diffraction (SAED) and X-ray energy dispersive spectroscopy (EDS), Mn K-edge X-ray absorption near-edge structure (XANES) spectroscopy, and acidic dissolution experiments. Finally, the As(III) adsorption behaviors on the Mn- or Al-incorporated Ox-GR samples were determined by batch adsorption kinetics combined with the release of SO_4^{2-}, Mn^{2+}, and Al^{3+} and partial products analyses with X-ray photoelectron spectroscopy (XPS) and As K-edge X-ray absorption spectroscopy (XAS).

2. Materials and methods

2.1. Synthesis of Mn- or Al-incorporated Ox-GR

The GR was synthesized by air oxidation of Fe^{2+} in the presence of sulfate and Mn^{2+} or Al^{3+}, with varying initial Fe/Mn molar ratios of 1, 6, and 24 and Fe/Al molar ratios of 6 and 36. A system with addition of Na_2SO_4 solution (Fe/Na molar ratio of 24) was used as control. Specifically, 10 mL $MeSO_4$ (Me = Mn, Al, or Na) with different concentrations was mixed with 90 mL of 0.211 mM NaOH and 90 mL of 0.127 mM $FeSO_4$ (OH/Fe = 1.66) in a 300 mL reaction cell. The mixed solution was oxidized in the open air under stirring at 25 °C. The suspension pH and redox potential (Eh) were monitored respectively with a pH electrode (Metrohm 6.0280.300) and a Pt electrode (Metrohm 6.0451.100), both of which referred to an Ag/AgCl reference electrode. The GR formed completely when the suspension pH and Eh curves reached the first inflection points (Christiansen et al., 2009) (arrow A in Fig. S1). Two mL of suspension was sampled at that time point and filtered through a 0.22 μm membrane for XRD analysis.

After the GR formed completely, 10 mL of 0.8 M HEPES was added to buffer the suspension pH (arrow B in Fig. S1), avoiding a sharp drop of suspension pH caused by the abundant H^+ release during GR oxidation. After stirring for ~3 min, 2.5 mL of 30% H_2O_2 was added to oxidize the GR (arrow C in Fig. S1). The oxidation reaction lasted for 40 min, during which 2 mL suspension were sampled at different time intervals and filtered through 0.22 μm membrane for XRD analysis. The specific variations of suspension pH and Eh during the formation of Ox-GR were described in the Electronic Supplementary Material (SM-1). The final Mn- or Al-incorporated Ox-GR suspension was centrifuged, washed, freeze dried, ground, and stored in a desiccator for subsequent characterizations.

2.2. Characterizations of Ox-GR

2.2.1. Acidic dissolution experiments

To obtain the chemical composition of Ox-GR samples, 10 mg dry sample was dissolved in 10 mL of 4 M HCl at 25 °C for 2 h. Additionally, acidic dissolution kinetics of two selected Ox-GR dried samples (*i.e.*, initial Fe/Mn = 24 and Fe/Al = 36) were examined to determine the dissolution rate and spatial distribution of Mn, Al, and SO_4^{2-} in the minerals. Briefly, 48 mg sample was dissolved in 150 mL of 2 M HCl for 2 h at 25 °C under stirring condition. At pre-set time intervals, 2.5 mL suspension was sampled and filtered through a 0.22 μm membrane filter. The concentrations of dissolved Fe, S, Mn, and Al in the filtrates were determined by inductively coupled plasma optical emission spectroscopy (ICP-OES).

2.2.2. XRD, FTIR, specific surface area, and Zeta potential

The XRD patterns of Ox-GR samples were measured with a Bruker D8 ADVANCE X-ray diffractometer (Cu Kα, λ = 0.15418 nm) with a scanning rate of 10°/min for the intermediate wet samples and 1°/min for the final dry samples at a step size of 0.02°. The wet samples were coated with a thin layer of glycerol to minimize oxidation during data collection (Hansen et al., 1994). The FTIR spectra of the dry samples, mixed with dry KBr (~1% sample weight), were measured over the wavenumber range of 4000–400 cm^{-1} with a resolution of 4 cm^{-1} and 64 scans against the air background (Bruker VERTEX 70). The specific surface area (SSA) of Ox-GR samples, determined by the five-point BET method, was measured using N_2 adsorption at 77 K (ASAP 2460, micromeritics) after vacuum degassing at 80 °C for 3 h. The Zeta potential of 2 g/L Ox-GR suspension, equilibrated at different pHs (pH 4–9) for 8 h in 0.05 M $NaNO_3$ solution, was measured using a Malvern Zetasizer ZEN 3600.

2.2.3. HRTEM-SAED-EDS and Mn K-edge XANES spectroscopic analyses

HRTEM images and SAED patterns of the Ox-GR samples were collected using a Talos F200S TEM. X-ray EDS were recorded using an

Oxford IE250 system. Mn K-edge XANES spectra were collected in fluorescence mode at beamline 1W2B of Beijing Synchrotron Radiation Facility (BSRF) using a Si(111) double crystal monochromator. Multiple scans (≥2) were conducted for each sample and the averaged spectra were used. All data were processed using software Athena (Ravel and Newville, 2005). The atomic fractions of Mn(II), Mn(III), and Mn(IV) in the Mn-incorporated Ox-GR were determined using the Combo method developed by Manceau et al. (2012), with an uncertainty of the Mn average valence being ~0.04. The spectra of Mn(II), Mn(III), and Mn(IV) reference compounds used for linear combination fitting (LCF) analysis were given in Fig. S2.

2.3. As(III) adsorption kinetics on the Ox-GR samples

As(III) adsorption kinetics were investigated by reacting 2 g/L Ox-GR with 1 mM As(III) at pH 5 ± 0.05 and 25 °C in 0.05 M $NaNO_3$ solution. The conditions were relevant to the weak acidic soil environments. The total suspension volume was 100 mL and the reaction lasted for 8 h under stirring condition. The mineral suspension (96.67 mL) was equilibrated at pH 5 and 0.05 M $NaNO_3$ for 10 h before addition of 3.33 mL of 30 mM As(III) solution. At regular time intervals, a 2 mL suspension was sampled and immediately filtered through a 0.22 μm membrane filter. The adsorption kinetics were conducted in duplicate. The concentrations of dissolved As, SO_4^{2-}, Mn, and Al were measured by ICP-OES. The amount of As adsorbed was calculated as the difference between the initial and remaining As in the solution. To determine whether As(III) was oxidized to As(V), 1 mL suspension after reaction for 8 h was mixed with 4 mL of 1 M NaOH in 10 mL tubes and shaken for 1 h. The dissolved As(V) after desorption was determined by the molybdate blue colorimetric method using a UV–vis spectrophotometer.

A pseudo-second-order kinetic equation was used to model the As adsorption kinetics:

$$\frac{d_{q_t}}{d_t} = k_2(q_e - q_t)^2 \quad (1)$$

Where the q_e and q_t are, respectively, the amount of As adsorbed (μmol/g) at equilibrium and an given time of t; k is the rate constant g/μmol/min. The linear equation of the pseudo-second-order kinetics can be obtained by integrating the above equation with the boundary conditions of $t = 0$, $q_t = 0$ and $t = t$, $q_t = q_e$:

$$\frac{t}{q_t} = \frac{1}{k_2 q_e^2} + \frac{t}{q_e} \quad (2)$$

The dry Ox-GR samples with Fe/Mn = 26 before and after As(III) adsorption were analyzed by XPS (VG Multilab2000) with an Al Kα X-ray source (1486 eV). The narrow spectral changes of Mn_{2p} and O_{1s} were scanned at a pass energy of 25 eV and an energy step size of 0.1 eV. Spectra were charge-corrected to C_{1s} with a binding energy of 284.80 eV collected from the surface adventitious carbon and analyzed with Advantage software. The As K-edge XAS of selected Ox-GR samples after As adsorption were collected in fluorescence mode at beamline 1W2B of BSRF. The data processing and analyses were given in the Supplementary Material (SM-2).

3. Results and discussion

3.1. Formation of Ox-GR in the presence of Mn or Al

The XRD patterns showed the characteristic peaks of GR(SO_4^{2-}) at d-spacing values of ~10.5 Å, ~5.4 Å, and ~ 3.6 Å (*i.e.*, black lines in Fig. 1a-1c) (Dideriksen et al., 2022; Perez et al., 2019), indicating the formation of GR at all conditions. Compared with the peak intensities of control system (Fig. 1a), the presence of Al^{3+} remarkably inhibited the crystallization of GR (Fig. 1c), consistent with the previous studies (Dideriksen et al., 2022; Refait et al., 2017; Ruby et al., 2008). After the addition of H_2O_2, the GR was quickly oxidized to Ox-GR, resulting in the rapid decrease of suspension pH and increase of suspension Eh (Fig. S1). The d-spacing of basal (001) plane of Ox-GR was slightly smaller than that of GR for the blank system (10.47 Å → 10.33 Å, Fig. 1a), but slightly larger than that of GR with the presence of Mn^{2+} (10.76 Å → 11.15 Å, Fig. 1b) or Al^{3+} (10.62 Å → 10.76 Å, Fig. 1c). The d-spacing of (001) plane of layered minerals (*e.g.*, GR, Ox-GR, LDH, and phyllosilicates) includes both layer thickness and interlayer distance (Bergaya and Lagaly, 2013), so the above variations might be caused by the following two reasons. One is that the suspension pH substantially decreases during the oxidation of GR to Ox-GR (Fig. S1), leading to more sulfate adsorption on the surfaces and/or enter into the interlayer (Wang et al., 2018), probably enlarging the interlayer distance; the other is that when Fe^{2+} and Mn^{2+} are oxidized to Fe(III) and Mn(III/IV) after GR oxidation, the Fe or Mn with a higher valence has a lower ionic radius compared to their divalent counterparts (Sposito, 2016) (Table S1), leading to the shrink of MeO_6 octahedra and thus decreasing the layer thickness. Noted that the slight shifts in the position of the (001) plane may be caused by the instrument error, which cannot be totally excluded due to the poorly crystalized property of GR, although our instrument was calibrated by corundum reference prior to the XRD measurements.

Compared with the diffraction peak intensities of GR for the blank and Fe/Mn = 24, the (001) plane of Ox-GR weakened and (002, 003) planes of Ox-GR even disappeared (Fig. 1a and b), suggesting the loss of periodicity to some extent along the c*-axis during GR oxidation. Additionally, the d-spacing of (001) plane of Ox-GR substantially decreased after sample drying (Fig. 1d-1f), similar to the formation of birnessite from buserite with drying (Feng et al., 2005), confirming the presence of water molecules in the interlayer. These water molecules probably form sulfate outer-sphere complexes with sulfate through hydrogen (H)-bonding (Wang et al., 2015), in addition to sulfate inner-sphere complexes, to stabilize the layer structure. Furthermore, the peak intensity of (001) plane (*i.e.*, c*-axis direction) decreased while those of a-b planes (*i.e.*, peaks at ~2.55 Å and ~ 1.48 Å) increased with drying (Fig. 1d-1f), probably ascribed to the change of preferred orientation and the slight structural rearrangement during sample washing and drying.

3.2. Chemical composition, SSA, and Zeta potential of Ox-GR samples

The chemical compositions of the dry Ox-GR samples showed that the Fe/Me ratios in the final products were higher than the initial values, especially for the Mn system (Table1), indicating that a certain amount of Mn/Al ions remained in the solution during the formation of Ox-GR, caused by the decrease of suspension pH (Fig. S1) that lead to the release of Mn/Al from minerals. Thus, the Fe/Me ratios in the final products were used to describe the samples, rather than the initial Fe/Me ratios. With increasing Mn or Al content in Ox-GR, the Me/S (Me = Fe + Mn/Al) molar ratios gradually decreased (Table1), suggesting that the presence of Mn or Al lead to more sulfate accumulated in the mineral, including surface adsorption and interlayer incorporation. Compared with the Mn system at the similar loading (*i.e.*, Fe/Me = 40), more sulfate were accumulated for the Al system (Table1), ascribed to the stronger interaction between sulfate and Al^{3+} (Sposito, 2016). The SSA of Ox-GR slightly increased from 61 m^2/g for Fe/Na = 24 to 68 m^2/g for Fe/Mn = 19 with increasing Mn content, while it firstly increased to 113 m^2/g for Fe/Al = 40 and then remarkably decreased to 37 m^2/g for Fe/Al = 6.3 with increasing Al content (Table1). The variation of SSA should be related to the different particle size, crystallinity, elemental composition and content, and particle aggregation of Ox-GR samples (Cornell and Schwertmann, 2003). The PZC of Ox-GR changed between 6.8 and 7.4, closing to the PZC value of single-sheet Ox-GR (*i.e.*, pH 7.8) (Yin et al., 2019b), and the presence of Mn or Al slightly enhanced its PZC, with the Mn system more obvious (Fig. S3).

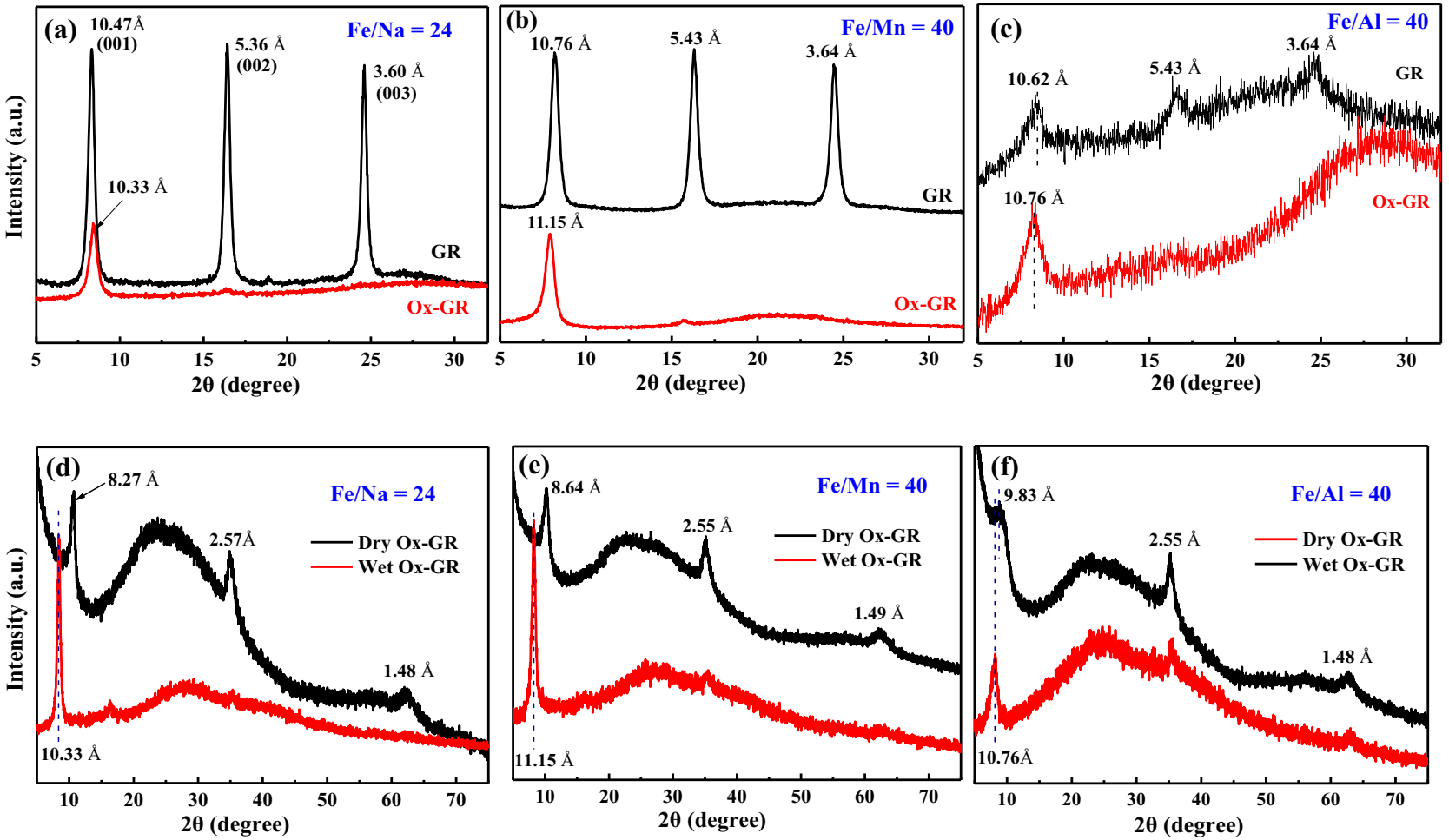

Fig. 1. XRD patterns of GR (black line) and its oxidation product of Ox-GR (red line) after adding H_2O_2 for ~40 min (a: Fe/Na = 24; b: Fe/Mn = 40; c: Fe/Al = 40) and XRD patterns comparison of wet (red line) and dry (black line) Ox-GR (d: Fe/Na = 24; e: Fe/Mn = 40; f: Fe/Al = 40). Noted that these XRD patterns were collected at the similar operation conditions, so their intensities were comparable. (For interpretation of the references to colour in this figure legend, the reader is referred to the web version of this article.)

3.3. Structure and morphology of Ox-GR samples

The XRD patterns of dry Ox-GR samples showed that the peak intensity and the full-width at half-maximum of Mn-bearing Ox-GR slightly increased compared to the blank Ox-GR (*i.e.*, Fe/Na = 24), but changed subtly with increasing Mn content (Fig. 2a-2d). In contrast, the crystallinity of Ox-GR decreased substantially with the presence of Al (Fig. 2a-2d). The diffraction peaks of Ox-GR with Fe/Al = 6.3 almost disappeared (Fig. 2a-2d), suggesting that the presence of Al remarkably enhanced the degree of structural disorder, leading to the stacking of only few Fe octahedral layers along the c*-axis. This should be ascribed to that the presence of Al substantially inhibits the crystal-growth of GR precursor (Fig. 1c) (Dideriksen et al., 2022; Refait et al., 2017), thus resulting in the poor crystalized of Ox-GR. In addition, with the increase of Mn or Al content, the d-spacing of (001) plane along the c-axis direction gradually shifted to a higher value (*i.e.*, lower 2θ angle) (Fig. 2a and b), which might involve the following two reasons. On one aspect, the incorporation of Mn or Al enhances the sulfate content (Table 1), probably resulting in the increase of interlayer sulfate density and thus enlarging the interlayer distance. On the other aspect, the electronegativity of Mn (1.55) and Al (1.61) is lower than that of Fe (1.83) (Sposito, 2016) (Table S1), so the electronegativity in each layer decreases after Mn or Al incorporation, resulting in weaker H-bonding between interlayer sulfate and layer Me-OH sites (*i.e.*, sulfate outer-sphere complex) (Liao et al., 2020), thus leading to an increase of interlayer distance.

On the contrary, with the increase of Mn or Al content, the d-spacing values of a-b plane shifted to a lower value (*i.e.*, higher 2θ angle) (Fig. 2c and d), most likely ascribed to the isomorphic substitution of Fe by Mn and Al. The ionic radii of Al(III) (0.54 Å) is lower than that of Fe(III) (0.65 Å), leading to the lattice contract and thus the decrease of unit-cell parameters and d-spacing, similar to that of Al-incorporated lepidocrocite (Liao et al., 2020). As to the Mn system, although Mn(III) and Fe(III) cations have similar ionic radii and charge (Table S1), the Mn(III) substitution may induce a decrease of in-plane unit-cell parameters owing to the Jahn-Teller distortion of Mn(III) octahedral (Alvarez et al., 2006), thus decreasing the d-spacing. Compared with the d-spacing values of Mn system, those of Al system showed more remarkably

Table 1
Chemical composition and SSA of the dry Mn- or Al-incorporated Ox-GR samples.

Initial Fe/Me ratios	Final Fe/Me ratios	Fe (mmol/g)	S (mmol/g)	Mn (mmol/g)	Al (mmol/g)	Molar ratios of (Fe + Mn/Al)/S	SSA (m^2/g)
Fe/Na = 24	/	10.1	1.25	/	/	8.1	61
Fe/Mn = 24	40	9.0	1.16	0.23	/	8.0	62
Fe/Mn = 6	26	9.2	1.31	0.35	/	7.3	68
Fe/Mn = 1	19	8.9	1.41	0.47	/	6.6	68
Fe/Al = 36	40	8.8	1.40	/	0.22	6.4	113
Fe/Al = 6	6.3	7.2	1.79	/	1.14	4.7	37

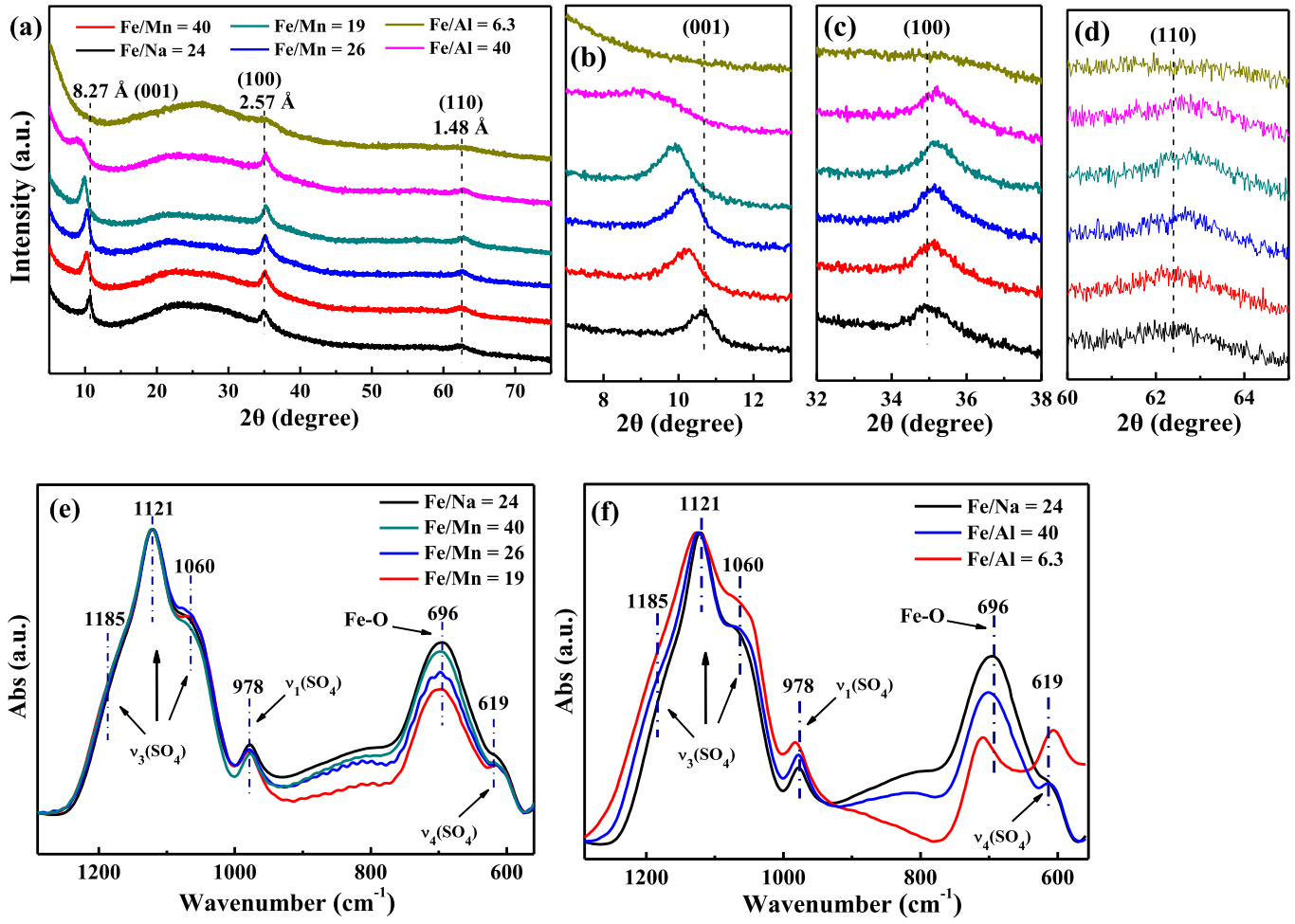

Fig. 2. The XRD patterns in the 2θ range of 5° – 75° (a), 7° – 13° (b), 32° – 38° (c), and 60° – 65° (d) and FTIR spectra (e: Mn system; f: Al system) of the dried Mn- or Al-incorporated Ox-GR samples.

variation (Fig. 2a-2d), due to the higher isomorphic substitution of Fe by Al (Table 1). Therefore, the incorporation of Mn or Al substantially modified the crystal structure of Ox-GR, with the Al system more obvious.

The SAED images of Ox-GR samples exhibited two polycrystalline rings (Fig. 3b-3f), corresponding to the two reflections of a-b plane (Fig. 2a). The calculated d-spacing values of a-b plane from the ED rings slightly decreased with the presence of Mn or Al (Fig. 3b-3e), consistent with the results of XRD patterns (Fig. 2a) and the lattice spacing analyses from the HRTEM images (Fig. S4a-S4d). In addition, the HRTEM images along the layer stacking direction showed that the d-spacing values of (001) plane are ~8.45 Å for Fe/Na = 24 (Fig. 3g) and ~ 8.75 Å for Fe/Mn = 19 (Fig. 3h), meaning that the presence of Mn increased the d-spacing of (001) plane, in agreement with the XRD results (Fig. 2a-2d). The small difference of the d-spacing values between XRD and TEM analyses probably comes from the calculation deviation due to the poor crystallinity of this mineral.

The FTIR spectra of the Ox-GR samples showed the characteristic Fe—O band at 696 cm^{-1} (Fig. 2e and f), which slightly shifted to a higher wavenumber with the presence of Mn or Al, especially for the Al system, probably due to the structural incorporation. The sulfate in Ox-GR exhibited asymmetric $\nu_3(SO_4)$ vibration bands at 1060 cm^{-1}, 1121 cm^{-1} and 1185 cm^{-1}, $\nu_1(SO_4)$ band at 978 cm^{-1},and $\nu_4(SO_4)$ band at 619 cm^{-1} (Fig. 2e and f), similar to the features of sulfate adsorption on hematite (Wang et al., 2018) and structural sulfate in schwertmannite (Wang et al., 2015). In addition, the $\nu_1(SO_4)$ band shifted to a higher

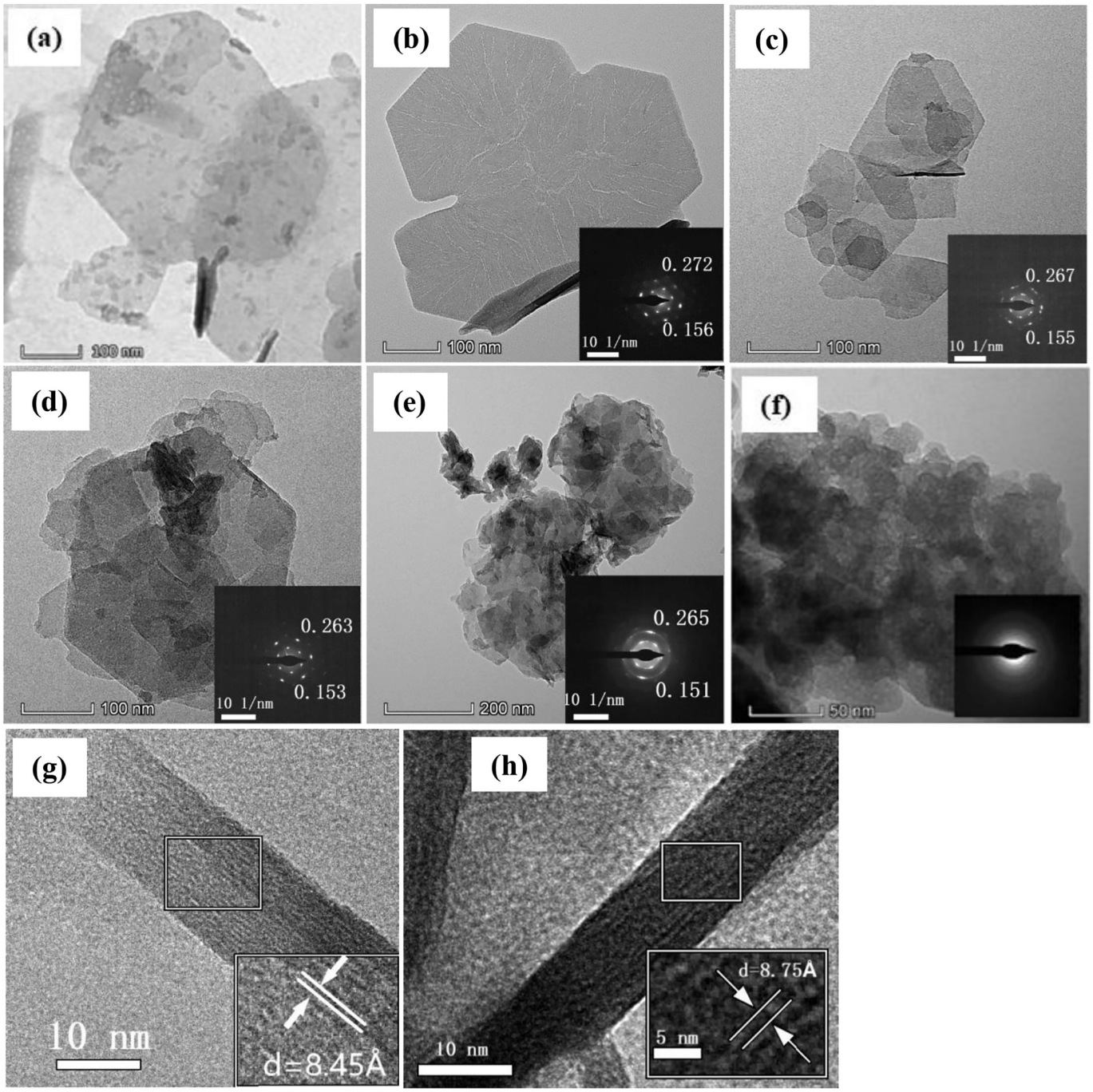

Fig. 3. The transmission electron microscope and selected-area electron diffraction images of GR (a) and Ox-GR samples (b: Fe/Na = 24; c: Fe/Mn = 40; d: Fe/Mn = 19; e: Fe/Al = 40; f: Fe/Al = 6.3); high-resolution transmission electron microscope images of c-axis direction of Ox-GR (g: Fe/Na = 24; h: Fe/Mn = 19).

wavenumber, while the $\nu_4(SO_4)$ band shifted to a lower wavenumber with increasing Mn or Al content (Fig. 2e and f), probably owing to partial SO_4 adsorption onto Mn-OH or Al-OH sites and/or the formation of Mn/Al-SO_4 ternary complexes on mineral edge surface (Johnston and Chrysochoou, 2016; Swedlund et al., 2009).

Besides the structure and composition variations, the presence of Mn or Al in Ox-GR also affected the particle morphology and size. The GR and Ox-GR crystals were approximately hexagonal flakes (Fig. 3a-3f). The particle surface of GR was smooth (Fig. 3a), while that of the Ox-GR showed some small cracks (Fig. 3b-3d). This might be due to that the *in-situ* oxidation of Fe^{2+} to Fe^{3+} decreases the ionic radius of Fe (*i.e.*, 0.078 nm for Fe^{2+} *versus* 0.065 nm for Fe^{3+}, Table S1), resulting in the lattice contraction and the increased degree of structural disorder at the c*-axis direction (Fig. 1a-1c). Compared to the blank sample, the presence of Mn or Al in Ox-GR reduced the particle size, with the Al system more obvious (Fig. 3b-3f), consistent with the XRD analyses (Fig. 2a). The Ox-GR particles for the Al system exhibited obvious aggregation features due to the small particle size (Fig. 3f). Therefore, the SSA increase of Ox-GR with Fe/Al = 40 should be due to the decrease of particle size and crystallinity, while the substantial decrease of SSA for the Ox-GR with Fe/Al = 6.3 is probably caused by the presence of abundant SO_4^{2-} (Table1) and remarkable particle aggregation (Fig. 3f) that could not be penetrated by N_2.

3.4. Speciation and distribution of Mn, Al, and sulfate in Ox-GR samples

The quantitative analyses of Mn K-edge XANES spectra showed that Mn mainly existed in the form of Mn(III) (~80%) in the Mn-bearing Ox-GR, with minor Mn(II) and little Mn(IV) (Fig. 4), indicating that most Mn (II) were oxidized to Mn(III) during the oxidation of GR to Ox-GR. The initial Mn concentration seemed no obvious effects on the proportion of different Mn valence in the final products (Fig. 4b).

The acidic dissolution kinetics of the products can reflect the elemental spatial distribution in the Ox-GR (Cornell and Schwertmann, 2003). The selected two Ox-GR samples (*i.e.*, Fe/Mn = 40 and Fe/Al = 40) were generally dissolved completely within 30 min, and the release kinetics of Fe, Mn, Al, and S from the mineral displayed a similar trend to each other (Fig. 5a and b). In addition, the release ratios of Mn, Al, and SO_4^{2-} all exhibited a positive linear correlation with that of Fe during the dissolution kinetics (Fig. 5c and d), indicating that Mn, Al, and S were largely uniformly distributed in the mineral structure, in addition to the surface adsorption. Consistently, the X-ray EDS mappings of Ox-GR samples showed that the elemental distribution of Fe, S, O, Mn, and Al basically coincided with the particle size and thickness, with thicker areas showing higher elemental contents (Fig. S5), further suggesting the homogenous distribution of these elements in the mineral.

The intercept of the fitted lines can roughly reflect the proportion of the ion adsorbed on mineral surfaces, with a larger intercept representing a higher proportion of adsorption (Cornell and Schwertmann, 2003). Accordingly, the fractions of sulfate and Mn located on mineral surface were, respectively, 0.22 and 0.1 for Fe/Mn = 40, while those of sulfate and Al were, respectively, 0.45 and 0.16 for Fe/Al = 40 (Fig. 5c and d). It means that Al incorporation led to a higher proportion of sulfate adsorption on the mineral surface than Mn incorporation at the similar Al/Mn loading. Considering that the intercepts of Mn and Al were relatively small (*i.e.*, 0.10 and 0.16) (Fig. 5c and d), majority of Mn and Al were distributed in the octahedral layers of the mineral.

3.5. Structural incorporation of Mn or Al into the Ox-GR

According to the analyses of XRD patterns (Fig. 2a-2d), FTIR spectra (Fig. 2e and f), X-ray EDS mapping (Fig. S5), and acid dissolution kinetics (Fig. 5), we can conclude that majority of Mn and Al were structurally incorporated into the layers of Ox-GR through isomorphous substitution, while SO_4^{2-} were distributed both on the mineral surface and in the interlayers of Ox-GR (Fig. 2e, f, and 5). The surface SO_4^{2-} likely formed binary and/or SO_4^{2-}-Mn^{2+}/Al^{3+} ternary complexes (Swedlund et al., 2009). The increased sulfate content in Ox-GR with Mn or Al incorporation (Table 1) might be related to the electrostatic attraction and/or the formation of SO_4^{2-}-Mn^{2+}/Al^{3+} ternary complexes on the mineral surface (probably minor in the interlayer). Compared with the Mn system, more sulfate adsorbed on the mineral surface for the Al system (Fig. 5), due to the stronger interaction between Al^{3+} and sulfate (Sposito, 2016). The Mn species that entered in the structure of Ox-GR was most likely Mn(III), probably with minor Mn(IV) (Fig. 4), due to the similar charge and ionic radius of Mn(III) and Fe(III) (Table S1), consistent with that of Mn incorporated into other Fe (oxyhydr)oxides (Cornell and Schwertmann, 2003).

3.6. As(III) adsorption-oxidation on Ox-GR samples

The As(III) adsorption kinetics on Ox-GR exhibited that arsenic adsorption increased rapidly in the initial stage, and then gradually reach an adsorption equilibrium within 8 h (Fig. 6a). To obtain the amount of As adsorbed at the equilibrium (q_e) and adsorption rate constant (k_2), the As adsorption kinetics were modeled by a pseudo-second-order equation as a previous study (Yin et al., 2019b), and the fitted results were summarized in Fig. 6b and Table S2. The high goodness of the fits ($R^2 > 0.95$) indicated that the As adsorption kinetics on Ox-GR can be described by the pseudo-second-order kinetic model (Table S2). Ascribed to the particle aggregation of Ox-GR (Fig. 3), their SSA will be underestimated through the measurement of N_2-BET method (Villalobos and Antelo, 2011), so we only compared the As(III) adsorption per mineral mass. Compared with the q_e of FeNa = 24 (*i.e.*,

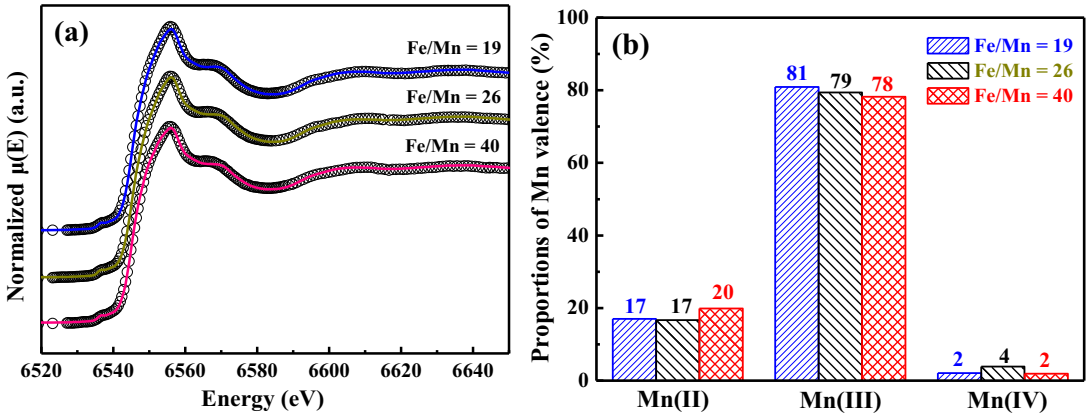

Fig. 4. The LCF fits of Mn K-edge XANES spectra (the circles are the experimental data, the lines are the best-fit data, and the bottom lines are the difference plots) (a) and the obtained atomic percentages of Mn(II), Mn(III), and Mn(IV) of Mn-incorporated Ox-GR (b).

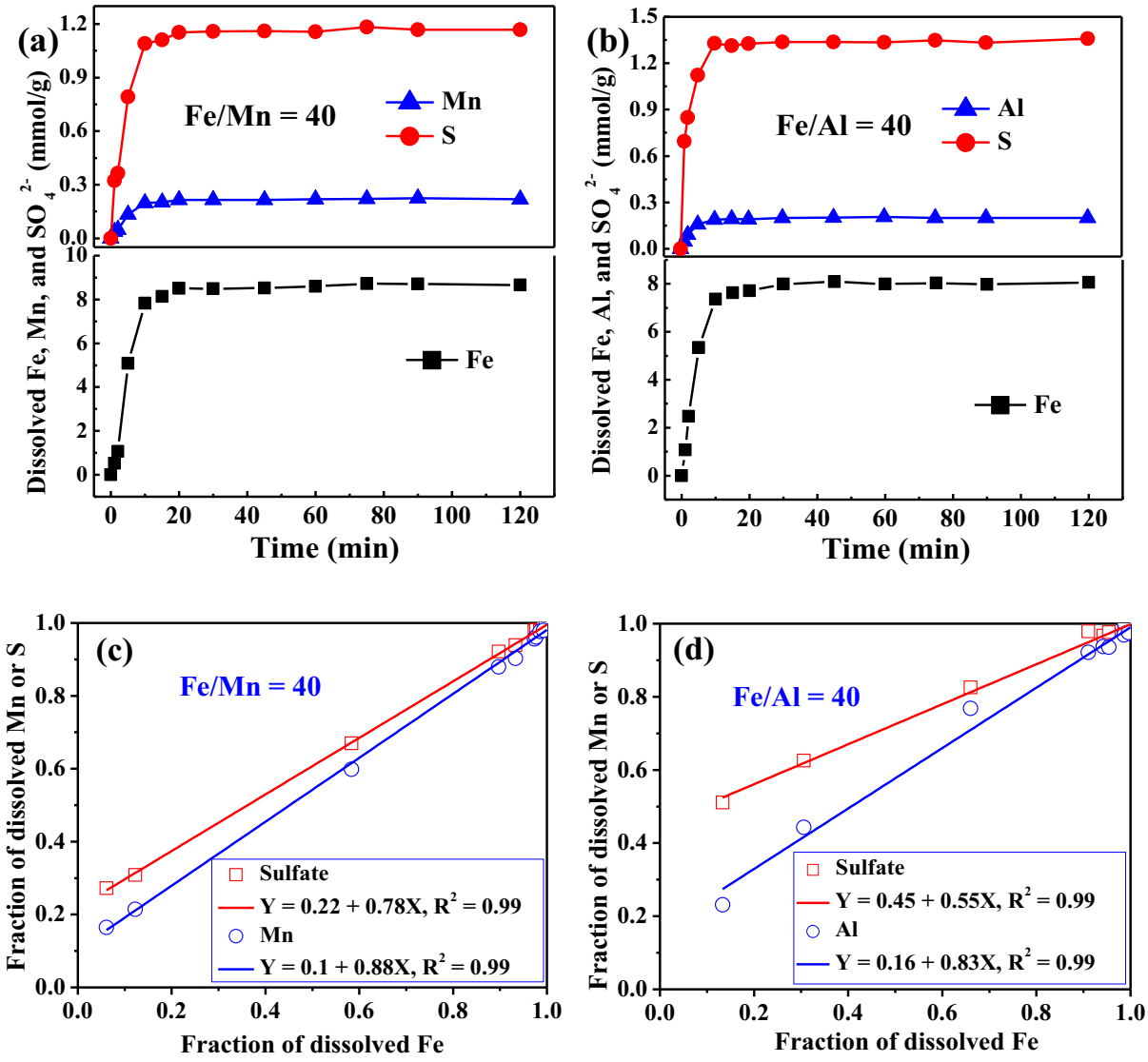

Fig. 5. Release kinetics of cations and sulfate (a: Fe/Mn = 40; b: Fe/Al = 40), and release proportion of cations and sulfate with the fraction of dissolved Fe for the final dried Ox-GR samples (c: Fe/Mn = 40; d: Fe/Al = 40) dissolved in 2 M HCl solution.

351 μmol/g), the incorporation of Mn and Al in Ox-GR both promoted the As adsorption. The q_e of Mn-bearing Ox-GR gradually increased from 364 μmol/g for Fe/Mn = 40 to 442 μmol/g for Fe/Mn = 19, while those of Al-incorporated Ox-GR were similar, *i.e.*, 429 μmol/g for Fe/Al = 40 and 429 μmol/g for Fe/Al = 6.3 (Table S2). Additionally, the obtained k_2 values of Ox-GR samples ranged from $3.90*10^{-4}$ to $5.02*10^{-4}$ g/μmol/min; the k_2 of Fe/Al = 40 was the highest while that of Fe/Al = 6.3 was the lowest (Table S2), probably depended on their SSA (Table 1). These fitted parameters of q_e and k_2 were comparable with those of As(V) adsorption on single-sheet Ox-GR (Yin et al., 2019b).

After As(III) adsorption by Ox-GR samples for 8 h, minor As(III) were oxidized to As(V), especially for the Mn system. The ratio of As(V)/total As in the suspension (including solution and solid) increased from 1.4% for Fe/Na = 24 to 22.4% for Fe/Mn = 19 and to 2.5% for Fe/Al = 6.3 (Fig. 6e), suggesting that the presence of Mn in Ox-GR remarkably promoted As(III) oxidation, while no promotion effects occurred for Al system. Although minor As(III) were oxidized to As(V) in the presence of Mn (Fig. 6e), As(III) was the main As species adsorbed on mineral surfaces (Fig. S6). The As K-edge EXAFS spectra of the Mn-incorporated Ox-GR samples after As(III) adsorption were shown in Fig. 7 and the fitted parameters were summarized in Table S3. The similar spectral features suggested little variation in the local coordination environment of As in the presence of Mn, despite partial oxidation. The dominant oscillatory pattern in the *k* space corresponded to the As—O peak in Fourier transform, fitted with $CN_{As\text{-}O}$ of 2.9–3.1 and an As—O bond length of 1.77 Å. The second peak mainly resulted from the multiple-scattering contribution of As-O-O, fitted with an average As-O-O distance of 3.22 Å. The third peak belonged to the As—Fe atomic pair, with the $CN_{As\text{-}Fe}$ ranging from 1.2 to 1.4 and an As—Fe interatomic distance of ~3.35 Å. This As—Fe interatomic distance was consistent with a bidentate-binuclear (BB) complex based on the geometric considerations (Jonsson and Sherman, 2008; Ona-Nguema et al., 2009; Perez et al., 2020).

The SO_4^{2-} release per mineral mass during kinetics gradually increased with increasing SO_4^{2-} content in Ox-GR and reaction time (Fig. 6c), generally consistent with that of As adsorption (Fig. 6a), suggesting that As adsorption on Ox-GR involved SO_4^{2-} exchange. The exchanged SO_4^{2-} should mainly come from the mineral surface rather than interlayer, since the preferred adsorption sites of As(III) are at the GR crystal edges (Perez et al., 2020). The O1s XPS fitting of the Ox-GR with Fe/Mn = 6 showed that after As adsorption the proportions of OH^- and H_2O decreased while that of lattice oxygen (O^{2-}) increased (Fig. 8a and b), indicating that As adsorption on Ox-GR also involved ligand exchange with surface Fe-OH/OH_2 groups (Perez et al., 2020; Yin et al.,

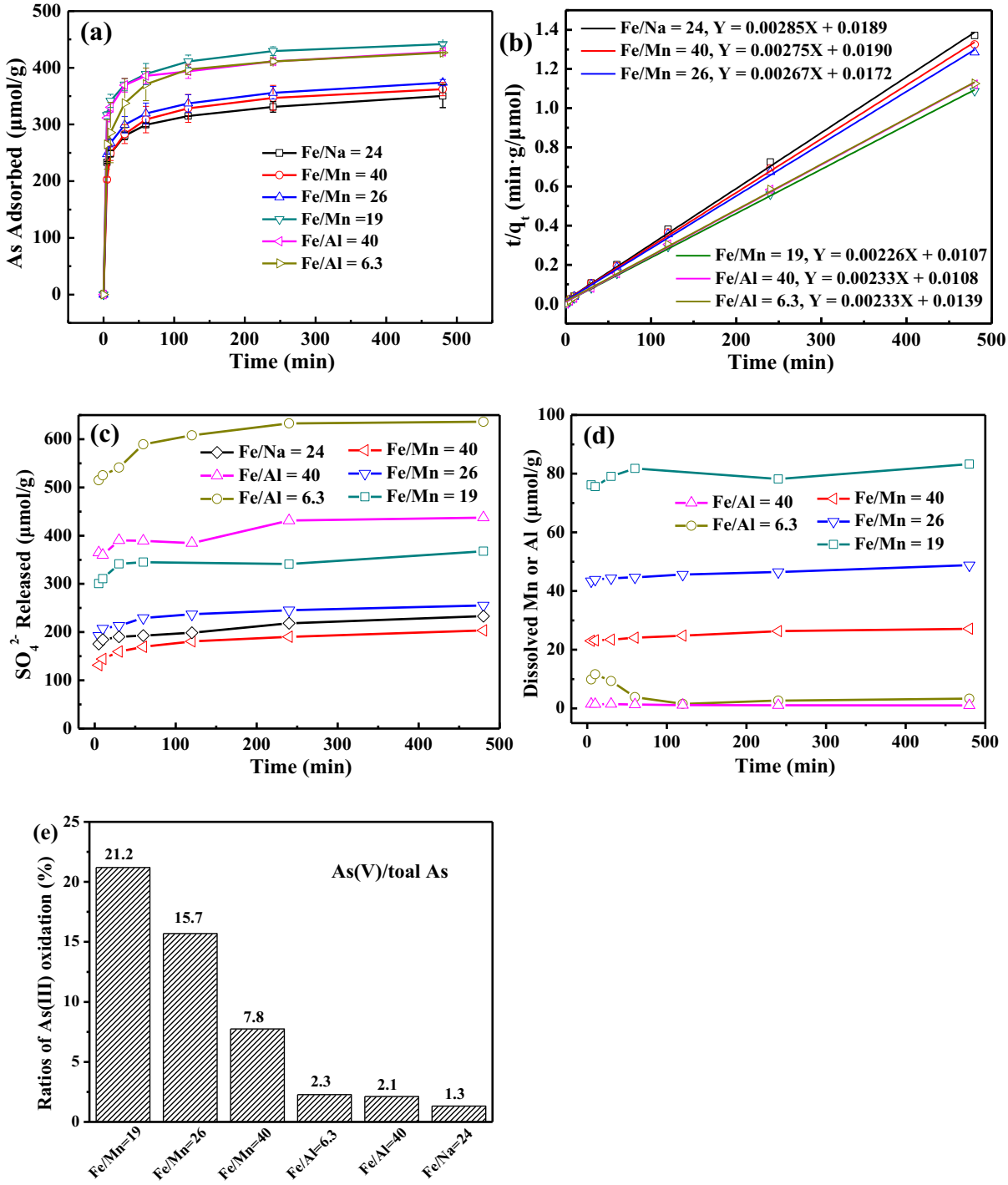

Fig. 6. The As(III) adsorption kinetics on Ox-GR samples at pH 5 (a) and pseudo second-order kinetic equation fitting normalized to mineral mass (b, $\frac{t}{q_t} = \frac{1}{k_2 q_e^2} + \frac{t}{q_e}$), and the dissolved SO_4^{2-} (c) and Mn and Al (d) during kinetics; the ratios of As(V)/total As in the suspension (including solution and solid) after As(III) adsorption for 8 h(e).

2019b). Therefore, the As adsorption on Ox-GR involved both anionic and ligand exchange.

The As adsorption promoted by the Mn or Al incorporation (Fig. 6a) thus can be explained by the following reasons. Firstly, Mn or Al incorporation in Ox-GR increased the SO_4^{2-} content (Table 1), prat of which can be anionic exchanged by As (Fig. 6c), thus a higher SO_4^{2-} content in Ox-GR brought more exchangeable adsorption sites and thus greater As adsorption. Secondly, the Mn or Al incorporation enhanced the SSA (except for Fe/Al = 6.3) (Table 1), providing more Fe-OH/OH_2 sites for As adsorption. Thirdly, Mn incorporation in Ox-GR promotes the oxidation of As(III) to As(V) (Fig. 6e), which enhanced the As adsorption because the As(V) exhibits a higher adsorption affinity on Fe oxide surface than As(III) at pH 5 (Dixit and Hering, 2003). Finally, the stacking disorder of Ox-GR remarkably increased with Al incorporation (Fig. 2a), allowing for higher proportion of sulfate bound to basal surface, thus favoring As(III) anionic exchange.

Accordingly, minor dissolved Mn and Al occurred during As adsorption (Fig. 6d). The dissolved Mn increased with increasing Mn content in Ox-GR, but it roughly keeps constant with reaction time (Fig. 6d). The dissolved Mn should be derived from desorption of surface

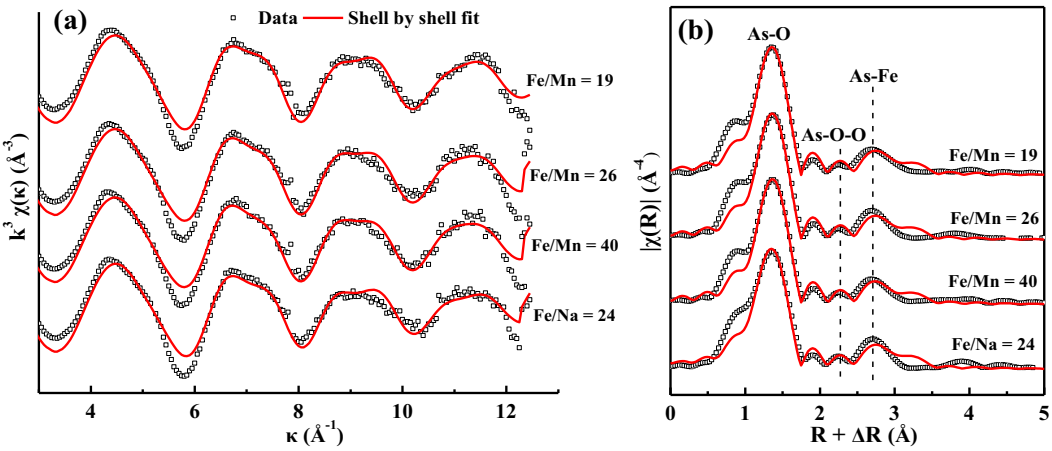

Fig. 7. As K-edge EXAFS spectroscopy for the data (blank square) and shell-by-shell model fits (red lines) for As(III) sorption kinetic samples (uncorrected for phase shifts): k^3-weighted χ(k) spectra (a) and Fourier transform magnitude (b), and the fitted parameters are summarized in Table S3. (For interpretation of the references to colour in this figure legend, the reader is referred to the web version of this article.)

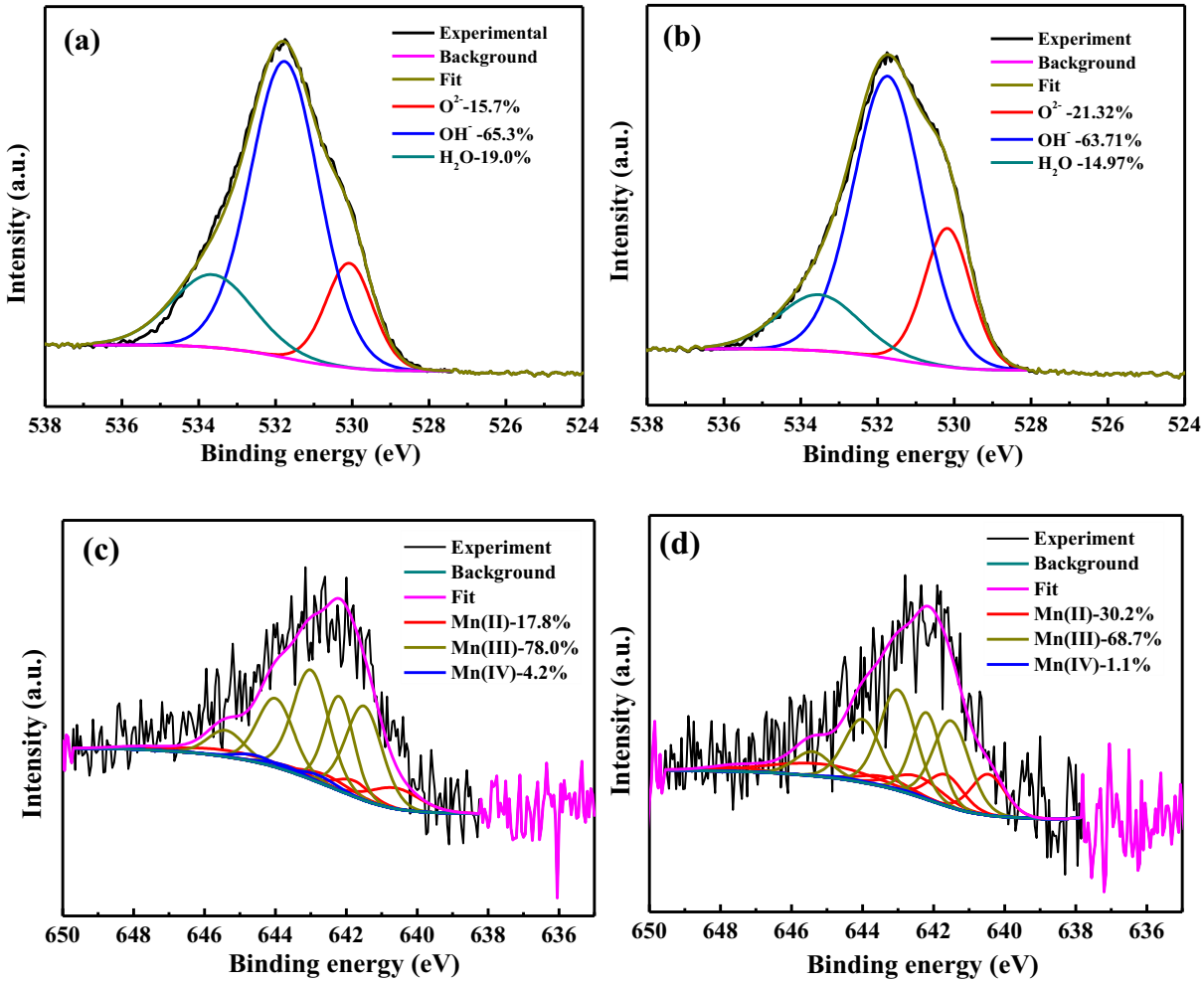

Fig. 8. Fitting results of O_{1s} and Mn_{2p} XPS of the Ox-GR sample with Fe/Mn = 26 before (a and c) and after (b and d) As(III) adsorption at pH 5.

adsorbed Mn^{2+} (Fig. 4b and 5c). In addition, the Mn2p XPS fitting of Fe/Mn = 6 indicates that partial Mn(III/VI) were reduced to Mn(II) during As(III) adsorption (Fig. 8c and d), which will lead to few Mn(II) release as well. In contrast, the Al is more difficult to release from mineral surface due to the higher adsorption affinity and hydrolysis constant of Al^{3+} (Sposito, 2016). Minor dissolved Al appeared at the beginning and then quickly re-adsorbed for the Ox-GR with Fe/Al = 6.3 (Fig. 6d), probably attributed to the increase of negative charge at the mineral surface after As adsorption that promotes Al^{3+} re-adsorption through electrostatic effects.

4. Conclusions

GR and its derivative Ox-GR are common in the subsurface environment, playing an extremely critical roles in regulating the biogeochemical processes of trace elements through interfacial reactions. The Ox-GR, a type of LDH mineral, is also an excellent adsorbent for removing contaminants from waste and drinking water (Barthelemy et al., 2012; Yin et al., 2019b). Our study systematically revealed the influence of Mn or Al incorporation on the structure, composition, elemental speciation and distribution, and As(III) adsorption of Ox-GR. The increase of sulfate content in Ox-GR with Mn or Al incorporation will decrease the mobility and availability of sulfate in the relevant environments and change the surface reactivity. The variations of crystal structure of Ox-GR with Mn or Al incorporation give us inspiration for understanding the structure of other LDH minerals with cation isomorphous substitution. Al incorporation substantially reduces the Fe octahedral layers of Ox-GR, leading to the formation of resemble "single-sheet" Ox-GR. The Mn or Al incorporation remarkably changes the structure, composition, and morphology of Ox-GR, promoting the As(III) adsorption of Ox-GR. The As adsorption mechanism involved a BB inner-sphere complex by exchanging both Fe–OH/OH_2 and sulfate groups, which is critical to constructing physically meaningful models. These new insights are essential to understanding the mineralogical properties and surface reactivity of naturally occurring Ox-GR. This study also provides a strategy for synthesis of poorly crystalline Ox-GR (*e.g.*, "single-sheet" mineral) for contaminant removal from wastewater.

Declaration of Competing Interest

The authors declare that they have no known competing financial interests or personal relationships that could have appeared to influence the work reported in this paper.

Data availability

Data will be made available on request.

Acknowledgments

The authors acknowledge the National Natural Science Foundation of China (No. 42030709 and 41977021), the National Key Research and Development Program of China (No. 2020YFC1806803), and the Fundamental Research Funds for the Central Universities (No. 2662019QD015).

Appendix A. Supplementary data

Electronic supplementary information (ESI) available: (1) variation of pH and Eh during the formation of EX-GR, (2) As K-edge XAS spectroscopy collection and analyses, (3) physicochemical properties of elements of Fe, Mn, and Al, (4) Fitting parameters of pseudo second-order kinetic equation and As K-edge EXAFS spectroscopy, (5) Zeta potential, TEM images and EDS mapping of Ox-GR samples, and (6) Mn references spectra. Supplementary data to this article can be found online at https://doi.org/10.1016/j.chemgeo.2022.121124.

References

Alvarez, M., Rueda, E.H., Sileo, E.E., 2006. Structural characterization and chemical reactivity of synthetic Mn-goethites and hematites. Chem. Geol. 231 (4), 288–299.
Ayala-Luis, K.B., Koch, C.B., Hansen, H.C.B., 2010. Intercalation of linear C9–C16 carboxylates in layered Fe^{II}–Fe^{III}-hydroxides (green rust) via ion exchange. Appl. Clay Sci. 48 (3), 334–341.
Barthelemy, K., Naille, S., Despas, C., Ruby, C., Mallet, M., 2012. Carbonated ferric green rust as a new material for efficient phosphate removal. J. Colloid Interface Sci. 384, 121–127.
Bergaya, F., Lagaly, G., 2013. Handbook of Clay Science (2nd, Developments in Clay Science). Elsevier.
Christiansen, B.C., Balic-Zunic, T., Petit, P.O., Frandsen, C., Morup, S., Geckeis, H., Katerinopoulou, A., Stipp, S.L.S., 2009. Composition and structure of an iron-bearing, layered double hydroxide (LDH) - green rust sodium sulphate. Geochim. Cosmochim. Acta 73 (12), 3579–3592.
Cornell, R.M., Schwertmann, U., 2003. The iron Oxides: Structure, Properties, Reactions, Occurrences and Uses, 2nd edition. Wiley-VCH, Weinheim, Germany.
Cruz, A., Cook, R.L., Dellinger, B., Lomnicki, S.M., Cosgriff, D., 2013. Assessment of environmentally persistent free radicals in soils and sediments from three superfund sites. Environ. Sci. Proc. Imp. 16 (1), 44–52.
Dideriksen, K., Voigt, L., Mangayayam, M.C., Eiby, S.H.J., van Genuchten, C.M., Frandsen, C., Jensen, K.M.Ø., Stipp, S.L.S., Tobler, D.J., 2022. Order and disorder in layered double hydroxides: lessons learned from the green rust sulfate-nikischerite series. ACS Earth Space Chem. 6 (2), 322–332.
Dixit, S., Hering, J.G., 2003. Comparison of arsenic(V) and arsenic(III) sorption onto iron oxide minerals: implications for arsenic mobility. Environ. Sci. Technol. 37 (18), 4182–4189.
Feng, X., Tan, W., Liu, F., Huang, Q., Liu, X., 2005. Pathways of birnessite formation in alkali medium. Sci. China Ser. D 48 (9), 1438–1451.
Feng, X., Wang, X., Zhu, M., Koopal, L.K., Xu, H., Wang, Y., Liu, F., 2015. Effects of phosphate and silicate on the transformation of hydroxycarbonate green rust to ferric oxyhydroxides. Geochim. Cosmochim. Acta 171, 1–14.
Genin, J.M.R., Ruby, C., 2004. Anion and cation distributions in Fe(II-III) hydroxysalt green rusts from XRD and Mossbauer analysis (carbonate, chloride, sulphate,…); the "fougerite" mineral. Solid State Sci. 6 (7), 705–718.
Hansen, H.C.B., Borggaard, O.K., Sørensen, J., 1994. Evaluation of the free energy of formation of Fe(II)-Fe(III) hydroxide-sulphate (green rust) and its reduction of nitrite. Geochim. Cosmochim. Acta 58 (12), 2599–2608.
Huang, L., Fang, L., Hassenkam, T., Dalby, K.N., Scheckel, K.G., Hansen, H.C.B., 2013. A one-step delamination procedure to form single sheet iron(III)-(oxy)hydroxides. J. Mater. Chem. A 1 (43), 13664–13671.
Inoue, K., Kwon, S.K., Kimijima, K., Kanie, K., Muramatsu, A., Shinoda, K., Suzuki, S., Waseda, Y., 2007. Analysis of iron oxyhydroxides and oxides converted from green rust in aqueous solution. ISIJ Int. 47 (3), 453–457.
Johnson, C.A., Freyer, G., Fabisch, M., Caraballo, M.A., Kusel, K., Hochella, M.F., 2014. Observations and assessment of iron oxide and green rust nanoparticles in metal-polluted mine drainage within a steep redox gradient. Environ. Chem. 11 (4), 377–391.
Johnson, C.A., Murayama, M., Kusel, K., Hochella, M.F., 2015. Polycrystallinity of green rust minerals and their synthetic analogs: implications for particle formation and reactivity in complex systems. Am. Mineral. 100 (10), 2091–2105.
Johnston, C.P., Chrysochoou, M., 2016. Mechanisms of chromate, selenate, and sulfate adsorption on Al-substituted ferrihydrite: implications for ferrihydrite surface structure and reactivity. Environ. Sci. Technol. 50 (7), 3589–3596.
Jonsson, J., Sherman, D.M., 2008. Sorption of as(III) and as(V) to siderite, green rust (fougerite) and magnetite: Implications for arsenic release in anoxic groundwaters. Chem. Geol. 255 (1–2), 173–181.
Jorand, F., Zegeye, A., Landry, F., Ruby, C., 2007. Reduction of ferric green rust by Shewanella putrefaciens. Lett. Appl. Microbiol. 45 (5), 515–521.
Legrand, L., Mazerolles, L., Chaussé, A., 2004. The oxidation of carbonate green rust into ferric phases:solid-state reaction or transformation via solution. Geochim. Cosmochim. Acta 68 (17), 3497–3507.
Liao, S., Wang, X., Yin, H., Post, J.F., Feng, X., 2020. Effects of Al substitution on local structure and morphology of lepidocrocite and its phosphate adsorption kinetics. Geochim. Cosmochim. Acta 276, 109–121.
Manceau, A., Marcus, M.A., Grangeon, S., 2012. Determination of Mn valence states in mixed-valent manganates by XANES spectroscopy. Am. Mineral. 97 (5–6), 816–827.
Ona-Nguema, G., Morin, G., Wang, Y.H., Menguy, N., Juillot, F., Olivi, L., Aquilanti, G., Abdelmoula, M., Ruby, C., Bargar, J.R., Guyot, F., Calas, G., Brown, G.E., 2009. Arsenite sequestration at the surface of nano-$Fe(OH)_2$, ferrous-carbonate hydroxide, and green-rust after bioreduction of arsenic-sorbed lepidocrocite by Shewanella putrefaciens. Geochim. Cosmochim. Acta 73 (5), 1359–1381.
Perez, J.P.H., Freeman, H.M., Schuessler, J.A., Benning, L.G., 2019. The interfacial reactivity of arsenic species with green rust sulfate ($GRSO_4$). Sci. Total Environ. 648, 1161–1170.
Perez, J.P.H., Freeman, H.M., Brown, A.P., van Genuchten, C.M., Dideriksen, K., S'Ari, M., Tobler, D.J., Benning, L.G., 2020. Direct visualization of arsenic binding on green rust sulfate. Environ. Sci. Technol. 54 (6), 3297–3305.
Perez, J.P.H., Tobler, D.J., Freeman, H.M., Brown, A.P., Hondow, N.S., van Genuchten, C.M., Benning, L.G., 2021. Arsenic species delay structural ordering during green rust sulfate crystallization from ferrihydrite. Environ. Sci. Nano.
Ravel, B., Newville, M., 2005. ATHENA, ARTEMIS, HEPHAESTUS: data analysis for X-ray absorption spectroscopy using IFEFFIT. J. Synchrotron Radiat. 12, 537–541.
Refait, P., Benali, O., Abdelmoula, M., Genin, J.M.R., 2003. Formation of 'ferric green rust' and/or ferrihydrite by fast oxidation of iron(II-III) hydroxychloride green rust. Corros. Sci. 45 (11), 2435–2449.
Refait, P., Reffass, M., Landoulsi, J., Sabot, R., Jeannin, M., 2007. Role of phosphate species during the formation and transformation of the Fe(II-III) hydroxycarbonate green rust. Colloids Surf. A Physicochem. Eng. Asp. 299 (1–3), 29–37.
Refait, P., Sabot, R., Jeannin, M., 2017. Role of Al(III) and Cr(III) on the formation and oxidation of the Fe(II-III) hydroxysulfate green rust. Colloids Surf. A Physicochem. Eng. Asp. 531, 203–212.
Ruby, C., Aïssa, R., Géhin, A., Cortot, J., Abdelmoula, M., Génin, J., 2006. Green rusts synthesis by coprecipitation of Fe^{II}–Fe^{III} ions and mass-balance diagram. Compt. Rendus Geosci. 338 (6–7), 420–432.

Ruby, C., Abdelmoula, M., Aissa, R., Medjahdi, G., Brunelli, M., Francois, M., 2008. Aluminium substitution in iron(II-III)-layered double hydroxides: Formation and cationic order. J. Solid State Chem. 181 (9), 2285–2291.
Sposito, G., 2016. The Chemistry of Soil, 3rd edition. Oxford University Press, New York, NY.
Su, C., Wilkin, R.T., 2005. Arsenate and arsenite sorption on and arsenite oxidation by iron(II, III) hydroxycarbonate green rust. In: O'Day, P. (Ed.), Advances in Arsenic Research. American Chemical Society, Washington, DC.
Swedlund, P.J., Webster, J.G., Miskelly, G.M., 2009. Goethite adsorption of Cu(II), Pb(II), Cd(II), and Zn(II) in the presence of sulfate: Properties of the ternary complex. Geochim. Cosmochim. Acta 73 (6), 1548–1562.
Tong, M., Yuan, S., Ma, S., Jin, M., Liu, D., Cheng, D., Liu, X., Gan, Y., Wang, Y., 2016. Production of abundant hydroxyl radicals from oxygenation of subsurface sediments. Environ. Sci. Technol. 50 (1), 214–221.
Trolard, F., Bourrié, G., 2006. Structure of fougerite and green rusts and a thermodynamic model for their stabilities. J. Geochem. Explor. 88 (1–3), 249–251.
Trolard, F., Génin, J.M.R., Abdelmoula, M., Bourrie, G., Herbillon, A., 1997. Identification of a green rust mineral in a reductomorphic soil by Mossbauer and Raman spectroscopies. Geochim. Cosmochim. Acta 61 (5), 1107–1111.
Usman, M., Byrne, J.M., Chaudhary, A., Orsetti, S., Hanna, K., Ruby, C., Kappler, A., Haderlein, S.B., 2018. Magnetite and green rust: synthesis, properties, and environmental applications of mixed-valent iron minerals. Chem. Rev. 118 (7), 3251–3304.
Villalobos, M., Antelo, J., 2011. A Unified Surface Structural Model for Ferrihydrite: Proton Charge, Electrolyte Binding, and Arsenate Adsorption. Revista Internacional De Contaminacion Ambiental 27 (2), 139–151.
Wang, X., Liu, F., Tan, W., Feng, X., Koopal, L.K., 2013. Transformation of hydroxycarbonate green rust into crystalline iron (hydr)oxides: influences of reaction conditions and underlying mechanisms. Chem. Geol. 351, 57–65.
Wang, X., Gu, C., Feng, X., Zhu, M., 2015. Sulfate local coordination environment in schwertmannite. Environ. Sci. Technol. 49 (17), 10440–10448.
Wang, X., Peng, J., Xu, H., Tan, W., Liu, F., Huang, Q., Feng, X., 2017. Influences and mechanisms of as(V) concentration and environmental factors on hydrosulfate green rust transformation. Acta Chim. Sin. 75 (6), 608–616.
Wang, X., Wang, Z., Peak, D., Tang, Y., Feng, X., Zhu, M., 2018. Quantification of coexisting inner- and outer-sphere complexation of sulfate on hematite surfaces. ACS Earth Space Chem. 2 (4), 387–398.
Wang, X., Peng, J., Liang, X., Zhu, M., Lanson, B., Wang, L., Liang, X., Liu, F., Tan, W., Feng, X., 2019. Effects of Mn^{2+}, Ni^{2+} and Cu^{2+} on the formation and transformation of hydrosulfate green rust: reaction processes and underlying mechanisms. ACS Earth Space Chem. 3, 519–530.
Yin, Z., Dideriksen, K., Abdelmoula, M., Ruby, C., Michel, F.M., Bjerrum, M.J., Hansen, H.C.B., 2019a. Structure of single sheet iron oxides produced from surfactant interlayered green rusts. Appl. Clay Sci. 170, 86–96.
Yin, Z., Lutzenkirchen, J., Finck, N., Celaries, N., Dardenne, K., Hansen, H.C.B., 2019b. Adsorption of arsenic(V) onto single sheet iron oxide: X-ray absorption fine structure and surface complexation. J. Colloid Interface Sci. 554, 433–443.